Sensorless self-commissioning of synchronous reluctance motors at standstill without rotor locking

Sensorless Self-Commissioning of Synchronous Reluctance Motors at Standstill Without Rotor Locking

Marko Hinkkanen, *Senior Member, IEEE,* Paolo Pescetto, Eemeli Mölsä, Seppo E. Saarakkala, Gianmario Pellegrino, *Senior Member, IEEE,* and Radu Bojoi, *Senior Member, IEEE*

***Abstract*—This paper proposes a standstill method for identification of the magnetic model of synchronous reluctance motors (SyRMs). The saturation and cross-saturation effects are properly taken into account. The motor is fed by an inverter with a short sequence of bipolar voltage pulses that are first applied on the rotor d- and q-axes separately and then simultaneously on both the axes. The stator flux linkages are computed by integrating the induced voltages. Using the current and flux samples, the parameters of an algebraic magnetic model are estimated by means of linear least squares. The proposed method is robust against errors in the stator resistance and inverter voltage, due to the high test voltages (of the order of the rated voltage). The fitted model matches very well with the reference saturation characteristics, measured using a constant-speed method, and enables extrapolation outside the sample range. The method was tested with a 2.2-kW SyRM, whose shaft was uncoupled from any mechanical load, which is the most demanding condition for this method. The proposed method can be used for automatic self-commissioning of sensorless SyRM drives at standstill.**

***Index Terms*—Flux maps, identification, linear least squares (LLS), saturation characteristics.**

I. Introduction

Synchronous reluctance motors (SyRMs) are simple to manufacture, mechanically robust, and comparatively cheap. If properly controlled using the maximum-torque-per-ampere (MTPA) principle, their efficiency is better (or their frame size is smaller) than that of the corresponding induction motor. In order to be able to replace general-purpose induction motor drives in simple applications (pumps, fans, conveyors, etc.), the SyRM drives should be sensorless. The MTPA principle and sensorless control require a magnetic model, where the cross-saturation must be properly taken into account. For general-purpose applications, the magnetic model of any unknown SyRM should be automatically identified at standstill during the drive start-up, using its power converter and embedded controller. This is a common practice in the case of induction motor drives, where various standstill self-commissioning algorithms have been available for the last 20 or more years, cf. e.g., [1], [2].

This work was supported in part by ABB Oy and in part by the Academy of Finland.

M. Hinkkanen, E. Mölsä, and S. E. Saarakkala are with the Department of Electrical Engineering and Automation, Aalto University, Espoo, Finland (e-mail: marko.hinkkanen@aalto.fi; olli.molsa@aalto.fi; seppo.saarakkala@aalto.fi).

P. Pescetto, G. Pellegrino, and R. Bojoi are with the Department of Energy, Politecnico di Torino, Turin, Italy (e-mail: paolo.pescetto@polito.it; gianmario.pellegrino@polito.it; radu.bojoi@polito.it).

An accurate way to identify the magnetic model of a SyRM is to rotate it at a constant speed in a test rig by another speed-controlled motor drive. The machine under test is current-controlled, and the flux linkages are calculated by means of the steady-state voltage equation. Such a constant-speed identification method can be considered as a reference method [3], [4], requiring a suitable test rig and off-line data processing. Based on similar principles as the constant-speed test, a self-commissioning procedure in [5] uses accelerations and decelerations to emulate loading conditions.

Dealing with standstill test conditions, several identification and self-commissioning methods for SyRMs and interior-permanent-magnet motors have been proposed recently [6]–[13]. The methods in [6]–[8] apply voltage (or current) steps to the machine under test and compute the stator flux linkage by integrating the induced stator voltage. Considering the d-axis as an example, the flux linkage ψ_d at standstill is

$$\psi_\mathrm{d}(t) = \int [u_\mathrm{d}(t) - R_\mathrm{s} i_\mathrm{d}(t)]\mathrm{d}t \tag{1}$$

where u_d is the voltage, i_d is the current, and R_s is the stator resistance. In [6]–[8], the applied voltage steps are selected so low that the steady state $u_\mathrm{d} = R_\mathrm{s} i_\mathrm{d}$ is reached, making the flux computation based on (1) highly sensitive to the stator resistance and inverter voltage.

In [12], the operating-point incremental inductances are explored using an AC current signal, superimposed to a DC bias emulating different operating points. The saturation curves are constructed from the estimated incremental inductances and the polarity of the DC bias is switched to achieve zero mean torque and no motion.

The method proposed in [13] is very simple and fast. It resembles the ones in [6]–[8], but uses bipolar voltage steps of much larger magnitude (up to the rated voltage), thus making the flux estimate practically insensitive to the stator resistance and offset errors. During a single voltage step, the whole range of currents is scanned and, unlike in [6]–[8], the steady state is not reached. In [13], the linear least squares (LLS) method was used to fit a piecewise-defined mathematical model to the measured samples. The cross-saturation effect is taken into account by dividing the cross-axis into segments, each of which has its own saturation curve and a set of fitted parameters. Overall, the method in [13] works well with self-axis identification, but the cross-saturation model is

impractical for its high number of parameters and its moderate accuracy.

In this paper [14], we propose a standstill identification method, which uses a similar excitation signal as the method in [13], with emphasis on improving the magnetic model. The algebraic magnetic model from [15] is adopted here, having a good trade-off between the number of parameters and accuracy. The standard LLS method is used for estimating the model parameters from the scattered current and flux data coming from the self-commissioning tests. The modelling approach was validated using the experimental data of five other SyRMs. Detailed simulation and experimental results are provided for the 2.2-kW SyRM drive to demonstrate the effectiveness of the proposed method. The saturation curves and MTPA trajectory obtained with the proposed self-commissioning method are compared with the reference data from constant-speed identification.

II. Motor Model

A. Fundamental Equations

The SyRM model in rotor coordinates is considered. The stator voltage equations are

$$\frac{\mathrm{d}\psi_\mathrm{d}}{\mathrm{d}t} = u_\mathrm{d} - R_\mathrm{s} i_\mathrm{d} + \omega_\mathrm{m}\psi_\mathrm{q} \tag{2a}$$

$$\frac{\mathrm{d}\psi_\mathrm{q}}{\mathrm{d}t} = u_\mathrm{q} - R_\mathrm{s} i_\mathrm{q} - \omega_\mathrm{m}\psi_\mathrm{d} \tag{2b}$$

where ψ_d and ψ_q are the flux-linkage components, u_d and u_q are the voltage components, ω_m is the electrical angular speed of the rotor, and R_s is the stator resistance. The current components

$$i_\mathrm{d} = i_\mathrm{d}(\psi_\mathrm{d}, \psi_\mathrm{q}) \qquad i_\mathrm{q} = i_\mathrm{q}(\psi_\mathrm{d}, \psi_\mathrm{q}) \tag{3}$$

are generally nonlinear functions of the flux components. They are the inverse of the flux maps extensively used in the literature [4]–[8], [12], [13], often represented by two-dimensional look-up tables. Here, the modelling approach (3) is chosen, because it is more favourable towards representation in the algebraic form. Since the nonlinear inductor should not generate or dissipate electrical energy, the reciprocity condition [16]

$$\frac{\partial i_\mathrm{d}(\psi_\mathrm{d}, \psi_\mathrm{q})}{\partial \psi_\mathrm{q}} = \frac{\partial i_\mathrm{q}(\psi_\mathrm{d}, \psi_\mathrm{q})}{\partial \psi_\mathrm{d}} \tag{4}$$

should hold. Typically, the core losses are either omitted or modelled separately using a core-loss resistor in the model. The produced torque is

$$T_\mathrm{e} = \frac{3p}{2}\left(\psi_\mathrm{d} i_\mathrm{q} - \psi_\mathrm{q} i_\mathrm{d}\right) \tag{5}$$

where p is the number of pole pairs. If the functions (3) and the stator resistance are known, the machine is fully characterized both in the steady and transient states. For example, the MTPA trajectory can be resolved from (3) and (5).

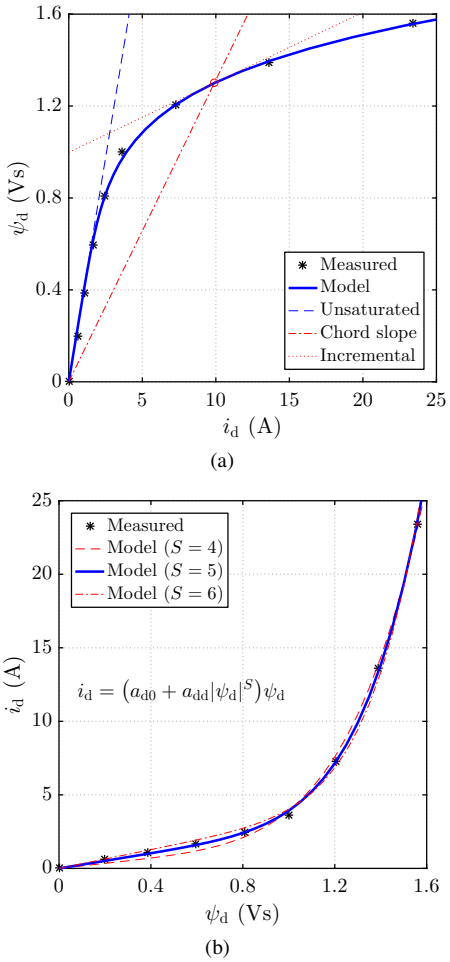

Fig. 1. Typical d-axis saturation characteristics at i_q = 0: (a) flux linkage $\psi_\mathrm{d} = \psi_\mathrm{d}(i_\mathrm{d})$; (b) current $i_\mathrm{d} = i_\mathrm{d}(\psi_\mathrm{d})$. In (a, b), the measured data points and the fitted model (7) for S = 5 are the same. In (a), the unsaturated inductance as well as the chord-slope inductance (8) and incremental inductance (9) at ψ_d = 1.3 Vs are shown. In (b), the rms residuals of the fitted models are 0.33 A (S = 4), 0.14 A (S = 5), and 0.36 A (S = 6).

B. Algebraic Magnetic Model

The use of a suitable algebraic magnetic model for (3) instead of look-up tables makes the self-commissioning problem easier. The number of parameters to be identified is reduced. The parameters are extracted by fitting the model to the data from a reduced number of tests, which reduces the duration of the commissioning and simplifies data processing. In the following, algebraic magnetic models will be introduced using the d-axis as an example. Then, the cross-saturation effect is included in the model.

1) Self-Axis Model: Fig. 1 shows typical d-axis saturation characteristics, when the q-axis current is zero. The data points shown in the figure have been measured from the 2.2-kW SyRM using the constant-speed method. The measured flux linkages as a function of the measured currents are shown in Fig. 1(a). The same measured data points are shown in the inverted coordinates in Fig. 1(b).

The characteristics $\psi_\mathrm{d} = \psi_\mathrm{d}(i_\mathrm{d})$ shown in Fig. 1(a), where the current i_d is the independent variable, are difficult to model with simple algebraic functions. Rational functions generally fit well to the measured data, but they may also

show vertical asymptotes or nonmonotonic behaviour, making the fitted function noninvertible.

For modeling the characteristics $i_\mathrm{d} = i_\mathrm{d}(\psi_\mathrm{d})$ shown in Fig. 1(b), a simple polynomial function could be used

$$i_\mathrm{d}(\psi_\mathrm{d}) = (a_{\mathrm{d}0} + a_{\mathrm{d}1}|\psi_\mathrm{d}| + \ldots + a_{\mathrm{d}n}|\psi_\mathrm{d}|^n)\,\psi_\mathrm{d} \tag{6}$$

where $a_{\mathrm{d}0} \ldots a_{\mathrm{d}n}$ are the coefficients and n is the highest exponent. The model is linear with respect to its coefficients, which makes it easy to use the LLS method. If n is high enough (typically n = 4...7 suffices), the polynomial function fits well to measured saturation data. Typically, some of the coefficients of the fitted polynomial tend to be negative, which may result in a nonmonotonic function outside the measured data range. To prevent this problem, more complicated constrained fitting methods could be used.

The polynomial function (6) can be simplified as [15], [17]

$$i_\mathrm{d}(\psi_\mathrm{d}) = \left(a_{\mathrm{d}0} + a_{\mathrm{dd}}|\psi_\mathrm{d}|^S\right)\psi_\mathrm{d} \tag{7}$$

where $a_{\mathrm{d}0}$ is the inverse of the unsaturated inductance, S is a positive exponent determining the shape of the saturation characteristics, and a_{dd} is a nonnegative coefficient. This function is monotonic and (numerically) invertible. The exponent S can be fixed and the LLS method can then be directly used. Rational numbers for S could be used, but integers were found out to give sufficient fit. Fig. 1(b) illustrates the effect of S on the LLS fit of (7) to the measured data. It can be seen (and calculated from the residuals) that S = 5 gives the best fit in this example. However, also S = 4 and S = 6 provide sufficient fit for practical purposes.

If needed, the model (7) can be expressed as an inductance function

$$L_\mathrm{d}(\psi_\mathrm{d}) = \frac{\psi_\mathrm{d}}{i_\mathrm{d}(\psi_\mathrm{d})} = \frac{1}{a_{\mathrm{d}0} + a_{\mathrm{dd}}|\psi_\mathrm{d}|^S} \tag{8}$$

which yields the chord-slope inductance as a function of ψ_d. The model (7) also inherently includes information of the incremental inductance

$$L_{\mathrm{di}}(\psi_\mathrm{d}) = \left[\frac{\partial i_\mathrm{d}(\psi_\mathrm{d})}{\partial \psi_\mathrm{d}}\right]^{-1} = \frac{1}{a_{\mathrm{d}0} + (S+1)a_{\mathrm{dd}}|\psi_\mathrm{d}|^S} \tag{9}$$

Examples of the chord-slope inductance (8) and incremental inductance (9) are shown in Fig. 1(a). To avoid confusions relating to various definitions of the inductances, the saturation characteristics are modeled using the form (3) in this paper.

The self-axis saturation characteristics of the q-axis can be modeled using the same function (with different parameters),

$$i_\mathrm{q}(\psi_\mathrm{q}) = \left(a_{\mathrm{q}0} + a_{\mathrm{qq}}|\psi_\mathrm{q}|^T\right)\psi_\mathrm{q} \tag{10}$$

Since the effective airgap is large along the q-axis, the exponent T = 1 typically suffices.

2) Inclusion of the Cross-Saturation: A form analogous to (7) is applied for modeling also the cross-saturation effect,

$$i_\mathrm{d}(\psi_\mathrm{d}, \psi_\mathrm{q}) = i_\mathrm{d}(\psi_\mathrm{d}, 0) + a'_{\mathrm{dq}}|\psi_\mathrm{d}|^U|\psi_\mathrm{q}|^{V'}\psi_\mathrm{d} \tag{11a}$$

$$i_\mathrm{q}(\psi_\mathrm{d}, \psi_\mathrm{q}) = i_\mathrm{q}(0, \psi_\mathrm{q}) + a'_{\mathrm{qd}}|\psi_\mathrm{d}|^{U'}|\psi_\mathrm{q}|^V\psi_\mathrm{q} \tag{11b}$$

where a'_{dq} and a'_{qd} are nonnegative coefficients and U, U', V, and V' are nonnegative exponents. The functions $i_\mathrm{d}(\psi_\mathrm{d}, 0)$ and $i_\mathrm{q}(0, \psi_\mathrm{q})$ describe the self-axis saturation characteristics, here modeled by (7) and (10), respectively. When taking the reciprocity condition (4) into account, the algebraic model (11) reduces to [15]

$$i_\mathrm{d}(\psi_\mathrm{d}, \psi_\mathrm{q}) = \left(a_{\mathrm{d}0} + a_{\mathrm{dd}}|\psi_\mathrm{d}|^S + \frac{a_{\mathrm{dq}}}{V+2}|\psi_\mathrm{d}|^U|\psi_\mathrm{q}|^{V+2}\right)\psi_\mathrm{d} \tag{12a}$$

$$i_\mathrm{q}(\psi_\mathrm{d}, \psi_\mathrm{q}) = \left(a_{\mathrm{q}0} + a_{\mathrm{qq}}|\psi_\mathrm{q}|^T + \frac{a_{\mathrm{dq}}}{U+2}|\psi_\mathrm{d}|^{U+2}|\psi_\mathrm{q}|^V\right)\psi_\mathrm{q} \tag{12b}$$

where $a_{\mathrm{d}0}$, a_{dd}, $a_{\mathrm{q}0}$, a_{qq}, and a_{dq} are nonnegative coefficients and S, T, U, and V are nonnegative exponents. There are three parameters for the d-axis, three for the q-axis, and three for the cross-saturation. The model is invertible, which makes it convenient to use. If desired, it could be expressed as inductance functions in a manner similar to (8) and (9).

The algebraic model (12) was further simplified by using only selected integers as exponents. In order to study the typical range of the exponents, the model was fitted to the saturation data of six different SyRMs, measured using the constant-speed method. The best fit exponents are given in Table I. It can be noticed that T = 1 and V = 0 hold for all the motors and U = 1 holds for five motors out of six. Optimal values of S vary between 5 and 8. Furthermore, a choice of S is not critical: the deviation of ± 1 from the optimal value still gives a good fit, as already illustrated in Fig. 1(b).

TABLE I
BEST FIT INTEGER EXPONENTS OF (12) FOR SIX SYRMS

Motor	Power (kW)	Speed (r/min)	S	T	U	V
CMP	0.9	3 600	6	1	1	0
EA3	2.2	1 500	5	1	1	0
EA4	4.0	1 500	5	1	1	0
ABB	6.7	1 500	6	1	1	0
PMP	7.5	1 500	8	1	3	0
Sicme	250	1 000	5	1	1	0

III. IDENTIFICATION METHOD AND MEASURED WAVEFORMS

A. Test Sequences

The test procedure proposed in [13] is briefly reviewed and illustrated with measured waveforms of a 2.2-kW SyRM drive. The rated line-line rms voltage of the motor is 400 V and the rated rms current is 5.1 A. Fig. 2 shows the sensorless controller used in the tests. The control scheme has been implemented on a dSPACE DS1103 board. The sampling of the currents is synchronized with the PWM operation. The sampling and switching period is T_s = 100 μs. In all the tests, the shaft of the motor was free (without any additional inertia connected to it) and no motion sensor was used. This condition is considered as the worst case for sensorless identification at standstill, since it is challenging to avoid that the current excitation makes the rotor move.

Only the initial position of the d-axis should be known, since it is assumed that the rotor does not considerably move during the test. If moving the rotor is possible, the DC-current

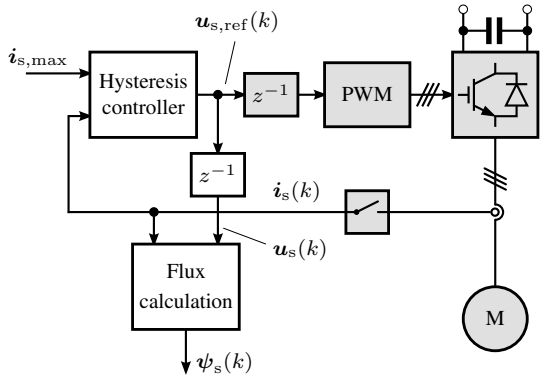

Fig. 2. Sensorless identification setup. The white blocks represent the control algorithm. The grey blocks model the plant: motor, converter, PWM, sampling, and computational time delay z^{-1}. The vector representation is used: $\boldsymbol{i}_{\mathrm{s}} = [i_{\mathrm{d}}, i_{\mathrm{q}}]^{\mathrm{T}}$, $\boldsymbol{u}_{\mathrm{s}} = [u_{\mathrm{d}}, u_{\mathrm{q}}]^{\mathrm{T}}$ and similarly for other vectors.

vector can be fed to the desired direction (e.g. the a-phase magnetic axis) before the test, which causes the rotor to rotate into this direction. Alternatively, the initial rotor position can be found using a signal-injection method, without causing the rotor movement. The results shown in the following were measured after parking the rotor using the DC current. The signal-injection method was also tested, as commented in the following.

1) d-Axis Test: A simple hysteresis controller is used. In the d-axis test, the control law is

$$u_{\mathrm{d,ref}}(k) = \begin{cases} u_{\mathrm{d,out}} & \text{if } i_{\mathrm{d}}(k) < -i_{\mathrm{d,max}} \\ -u_{\mathrm{d,out}} & \text{if } i_{\mathrm{d}}(k) > i_{\mathrm{d,max}} \\ u_{\mathrm{d,ref}}(k-1) & \text{otherwise} \end{cases} \tag{13a}$$

$$u_{\mathrm{q,ref}}(k) = 0 \tag{13b}$$

where $u_{\mathrm{d,out}}$ is the test-voltage magnitude, $i_{\mathrm{d,max}}$ is the current limit, and k is the discrete-time index. The current limit defines the current span, i.e. the range of identification. It can be selected to be, e.g., twice the rated current. In the d-axis test, the torque is ideally zero and the operating point is stable even at free shaft.

Fig. 3(a) shows the measured waveforms of the d-axis test. The samples of two complete cycles, shown in the figure, are used in the identification. The zero-crossings are detected from the reference voltage $u_{\mathrm{d,ref}}(k)$. The data of one complete cycle would suffice for identification, but two cycles are used here for better illustration. The test voltage is $u_{\mathrm{d,out}}$ = 200 V and the current limit is $i_{\mathrm{d,max}}$ = 20 A (which is almost three times the rated current).

2) q-Axis Test: The control law in the q-axis test is analogous to (13). The torque is ideally zero also in the q-axis test, but the operating point is only marginally stable. If the rotor is free to rotate, the current limit $i_{\mathrm{q,max}}$ should be selected low enough to avoid the rotor movement. Fig. 3(b) shows the measured waveforms of the q-axis test. As in the case of the d-axis test, the samples of two complete cycles are shown and used in the identification. The test voltage is $u_{\mathrm{q,out}}$ = 200 V and the current limit is $i_{\mathrm{q,max}}$ = 14 A. As the rotor was positioned with the DC current before the test, this test condition could be used for several seconds

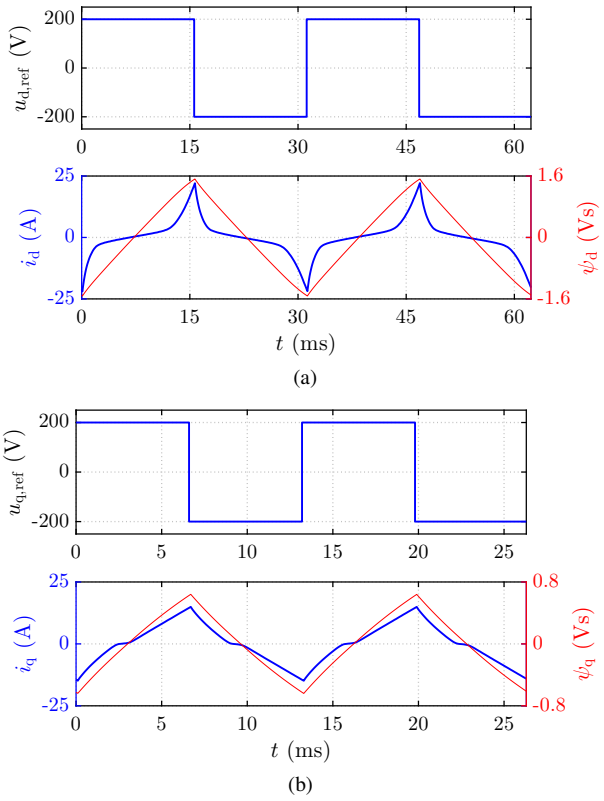

Fig. 3. Measured self-axis test waveforms: (a) d-axis; (b) q-axis. The upper subplots show the voltages. The lower subplots show the measured currents and the calculated fluxes. The parameters are $u_{\mathrm{d,out}} = u_{\mathrm{q,out}}$ = 200 V, $i_{\mathrm{d,max}}$ = 20 A, and $i_{\mathrm{q,max}}$ = 14 A. The number of samples is N_{d} = 624 in the d-axis test and N_{q} = 264 in the q-axis test.

without the rotor movement. Instead, when the initial rotor position was estimated using signal injection and $i_{\mathrm{q,max}}$ = 14 A was used, the rotor moved less than five electrical degrees during the first two complete cycles, due to inaccuracies in the initial position estimate and the voltage production. The rotor movement can be decreased or avoided by decreasing the limit $i_{\mathrm{q,max}}$. Alternatively, if the rotor moves during the q-axis test, it means that the rotor can be parked into a more stable initial position, and the test can be repeated using the full current range (14 A in this case).

3) Cross-Saturation Test: The hysteresis controllers corresponding to (13a) are simultaneously used in the d- and q-axes. The torque varies during the test, but the average torque is approximately zero. Fig. 4 shows the measured waveforms of the cross-saturation test. The samples of two complete d-axis cycles are used in the identification. The test voltages are 200 V and the current limits are $i_{\mathrm{d,max}}$ = 20 A and $i_{\mathrm{q,max}}$ = 8 A. During the sequence shown in Fig. 4, the rotor angle varied less than 10 electrical degrees. When the initial rotor position was detected using signal injection, the same current limits could be used.

The test-voltage magnitude is limited by the DC-bus voltage U_{dc} of the inverter, i.e., $u_{\mathrm{d,out}}^2 + u_{\mathrm{q,out}}^2 < U_{\mathrm{dc}}^2/3$. The higher is the test voltage, the less variation there will be in the rotor speed and angle during the cross-saturation test (for the same current limits). This effect of the test-voltage magnitude on the rotor movement is also verified by means of simulations

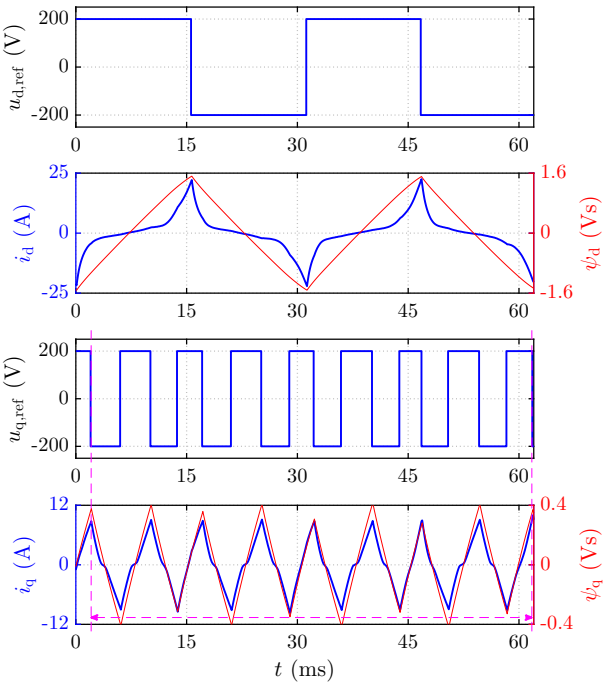

Fig. 4. Measured waveforms of the cross-saturation test, where both the axes are simultaneously excited. The first two subplots show the data for the d-axis and the last two subplots show the data for the q-axis. The parameters are $u_{\mathrm{d,out}} = u_{\mathrm{q,out}} = 200$ V, $i_{\mathrm{d,max}} = 20$ A, and $i_{\mathrm{q,max}} = 8$ A. The number of samples is $N_{\mathrm{dq}} = 621$. The average value of the q-axis flux was calculated from the complete cycles (the interval t = 2.0. . .61.8 ms marked in the figure).

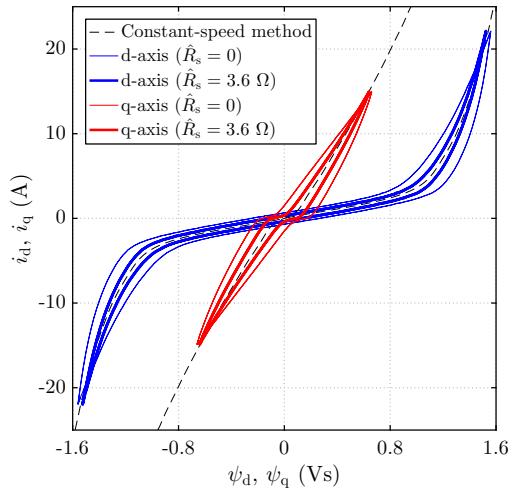

Fig. 5. Measured self-axis saturation characteristics, when $\hat{R}_{\mathrm{s}} = 0$ and $\hat{R}_{\mathrm{s}} = 3.6\ \Omega$ are used in the flux calculation (14). In neither cases are the inverter nonlinearities compensated for. The data of the curves for $\hat{R}_{\mathrm{s}} = 3.6\ \Omega$ is the same as in Fig. 3. The dashed lines show the reference saturation curves, measured using the constant-speed method.

in Section V. It is worth noticing that bigger machines have higher per-unit rotor inertia, which helps reducing the variation of the rotor during the test.

B. Flux Calculation

The flux linkages are calculated using the forward Euler approximation

$$\psi_{\mathrm{d}}(k+1) = \psi_{\mathrm{d}}(k) + T_{\mathrm{s}}[u_{\mathrm{d}}(k) - \hat{R}_{\mathrm{s}} i_{\mathrm{d}}(k)] \qquad (14)$$

In order to compensate for the computational time delay of one sampling period, the voltage $u_{\mathrm{d}}(k) = u_{\mathrm{d,ref}}(k-1)$ is used in the flux calculation. The analogous equation is used for the q-axis. The estimate $\hat{R}_{\mathrm{s}}$ for the stator resistance is obtained simply by feeding the DC current into the stator before the test sequences. Unless otherwise noted, the measured value $\hat{R}_{\mathrm{s}} = 3.6\ \Omega$ is used. Inverter nonlinearities could be identified and compensated for, but they are omitted in this paper because the proposed method works fine also without the compensation.

In the self-axis tests, the samples consist of complete cycles. The average of the flux samples is calculated and removed from the samples. Fig. 3 shows the waveforms of the calculated flux samples after the average value has been removed. Using the same data, the currents are plotted as functions of the fluxes in Fig. 5. It can be seen that the two cycles almost perfectly overlap. The dashed lines in the figure show the reference saturation curves, which have been measured using the constant-speed method [4]. For $\hat{R}_{\mathrm{s}} = 3.6\ \Omega$, the hysteretic behavior mainly originates from the core losses of the motor and from the uncompensated inverter nonlinearities. If $\hat{R}_{\mathrm{s}} = 0$ is used in (14), the hysteresis loops become slightly thicker, but their shape remains similar, as also shown in Fig. 5. The hysteretic behaviour, however, has a minor effect on the accuracy of the identified magnetic model, as will be seen later in the paper.

In the cross-saturation test, the d-axis samples have complete cycles, but the q-axis samples generally include an incomplete cycle (in addition to several complete cycles), which may distort the average. Hence, to minimize this distortion, the average value of the q-axis flux is calculated using only the complete cycles (cf. the interval marked with the vertical dashed lines in Fig. 4) and removed from all the samples.

C. LLS Method

If the exponents of the magnetic model (12) are fixed, the remaining five parameters can be conveniently estimated using the standard LLS method. The estimation problem reduces to solving a set of linear equations: there is a unique solution and neither initial values nor cost functions are needed. A recursive variant [18] of LLS can be easily implemented in embedded processors used in converters. Since the amount of feasible integer exponents is limited, as discussed in Section II-B, the parameters can be solved for different sets of exponents, which have been chosen in advance. Then, the set of exponents (and the corresponding fitted parameters) leading to the smallest sum of the squared residuals can be chosen. The data collected during the three tests (d-axis, q-axis, and cross-saturation tests) are used in three consecutive fits, as explained below.

1) d-Axis Fit: Assuming positive current and flux samples, the model (12) for the d-axis reduces to

$$i_{\mathrm{d}} = a_{\mathrm{d0}} \psi_{\mathrm{d}} + a_{\mathrm{dd}} \psi_{\mathrm{d}}^{S+1} \qquad (15)$$

when only the d-axis is excited. If the exponent S is fixed, this model is linear with respect to the unknown parameters

TABLE II
FITTED PARAMETERS GIVEN IN SI UNITS

S	T	U	V	$a_{\mathrm{d}0}$	a_{dd}	$a_{\mathrm{q}0}$	a_{qq}	a_{dq}
5	1	1	0	2.41	1.47	12.8	17.0	13.2

$a_{\mathrm{d}0}$ and a_{dd}. The LLS problem in a vector form is

$$\underbrace{\begin{bmatrix} i_{\mathrm{d}}(1) \\ i_{\mathrm{d}}(2) \\ \vdots \\ i_{\mathrm{d}}(N_{\mathrm{d}}) \end{bmatrix}}_{\boldsymbol{y}_{\mathrm{d}}} = \underbrace{\begin{bmatrix} \psi_{\mathrm{d}}(1) & \psi_{\mathrm{d}}(1)^{S+1} \\ \psi_{\mathrm{d}}(2) & \psi_{\mathrm{d}}(2)^{S+1} \\ \vdots & \vdots \\ \psi_{\mathrm{d}}(N_{\mathrm{d}}) & \psi_{\mathrm{d}}(N_{\mathrm{d}})^{S+1} \end{bmatrix}}_{\boldsymbol{X}_{\mathrm{d}}} \underbrace{\begin{bmatrix} a_{\mathrm{d}0} \\ a_{\mathrm{dd}} \end{bmatrix}}_{\boldsymbol{\beta}_{\mathrm{d}}} + \underbrace{\begin{bmatrix} \varepsilon_{\mathrm{d}}(1) \\ \varepsilon_{\mathrm{d}}(2) \\ \vdots \\ \varepsilon_{\mathrm{d}}(N_{\mathrm{d}}) \end{bmatrix}}_{\boldsymbol{\varepsilon}_{\mathrm{d}}} \tag{16}$$

where $\boldsymbol{y}_{\mathrm{d}}$ is the vector of the current samples, $\boldsymbol{X}_{\mathrm{d}}$ is regressor matrix, $\boldsymbol{\beta}_{\mathrm{d}}$ is the parameter vector, $\boldsymbol{\varepsilon}_{\mathrm{d}}$ is the residual vector, and N_{d} is the number of samples. The sum of the squared residuals is

$$J_{\mathrm{d}}(\boldsymbol{\beta}_{\mathrm{d}}) = \boldsymbol{\varepsilon}_{\mathrm{d}}^{\mathrm{T}} \boldsymbol{\varepsilon}_{\mathrm{d}} \tag{17}$$

The parameter vector minimizing J_{d} is

$$\boldsymbol{\beta}_{\mathrm{d}} = (\boldsymbol{X}_{\mathrm{d}}^{\mathrm{T}} \boldsymbol{X}_{\mathrm{d}})^{-1} \boldsymbol{X}_{\mathrm{d}}^{\mathrm{T}} \boldsymbol{y}_{\mathrm{d}} \tag{18}$$

The fitting can be carried out using pre-selected values for the exponent S, and the best value can be chosen based on (17).

2) q-Axis Fit: The parameters estimation procedure for the q-axis is fully analogous to the that of the d-axis. The parameter vector is $\boldsymbol{\beta}_{\mathrm{q}} = [a_{\mathrm{q}0}, a_{\mathrm{qq}}]^{\mathrm{T}}$ and the number of samples is N_{q}.

3) Cross-Saturation Fit: The model (12) can be rewritten as

$$i_{\mathrm{d}} - a_{\mathrm{d}0}\psi_{\mathrm{d}} - a_{\mathrm{dd}}\psi_{\mathrm{d}}^{S+1} = \frac{a_{\mathrm{dq}}}{V+2}\psi_{\mathrm{d}}^{U+1}\psi_{\mathrm{q}}^{V+2} \tag{19a}$$

$$i_{\mathrm{q}} - a_{\mathrm{q}0}\psi_{\mathrm{q}} - a_{\mathrm{qq}}\psi_{\mathrm{q}}^{T+1} = \frac{a_{\mathrm{dq}}}{U+2}\psi_{\mathrm{d}}^{U+2}\psi_{\mathrm{q}}^{V+1} \tag{19b}$$

Since the parameters $a_{\mathrm{d}0}$, a_{dd}, $a_{\mathrm{q}0}$, and a_{qq} are known, the output vector

$$\boldsymbol{y}_{\mathrm{dq}} = \begin{bmatrix} i_{\mathrm{d}}(1) - a_{\mathrm{d}0}\psi_{\mathrm{d}}(1) - a_{\mathrm{dd}}\psi_{\mathrm{d}}(1)^{S+1} \\ i_{\mathrm{q}}(1) - a_{\mathrm{q}0}\psi_{\mathrm{q}}(1) - a_{\mathrm{qq}}\psi_{\mathrm{q}}(1)^{T+1} \\ \vdots \\ i_{\mathrm{d}}(N_{\mathrm{dq}}) - a_{\mathrm{d}0}\psi_{\mathrm{d}}(N_{\mathrm{dq}}) - a_{\mathrm{dd}}\psi_{\mathrm{d}}(N_{\mathrm{dq}})^{S+1} \\ i_{\mathrm{q}}(N_{\mathrm{dq}}) - a_{\mathrm{q}0}\psi_{\mathrm{q}}(N_{\mathrm{dq}}) - a_{\mathrm{qq}}\psi_{\mathrm{q}}(N_{\mathrm{dq}})^{T+1} \end{bmatrix} \tag{20}$$

is chosen, where N_{dq} is the number of samples. The regressor matrix is

$$\boldsymbol{X}_{\mathrm{dq}} = \begin{bmatrix} \frac{1}{V+2}\psi_{\mathrm{d}}(1)^{U+1}\psi_{\mathrm{q}}(1)^{V+2} \\ \frac{1}{U+2}\psi_{\mathrm{d}}(1)^{U+2}\psi_{\mathrm{q}}(1)^{V+1} \\ \vdots \\ \frac{1}{V+2}\psi_{\mathrm{d}}(N_{\mathrm{dq}})^{U+1}\psi_{\mathrm{q}}(N_{\mathrm{dq}})^{V+2} \\ \frac{1}{U+2}\psi_{\mathrm{d}}(N_{\mathrm{dq}})^{U+2}\psi_{\mathrm{q}}(N_{\mathrm{dq}})^{V+1} \end{bmatrix} \tag{21}$$

The cross-saturation parameter is estimated as

$$a_{\mathrm{dq}} = (\boldsymbol{X}_{\mathrm{dq}}^{\mathrm{T}} \boldsymbol{X}_{\mathrm{dq}})^{-1} \boldsymbol{X}_{\mathrm{dq}}^{\mathrm{T}} \boldsymbol{y}_{\mathrm{dq}} \tag{22}$$

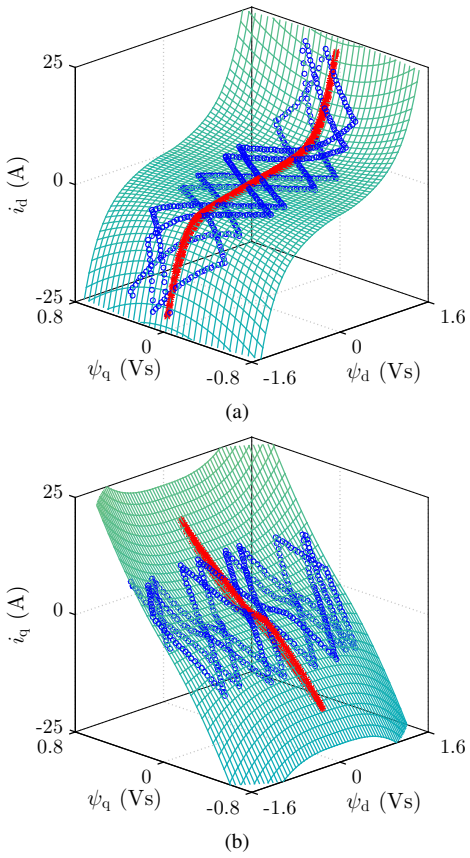

Fig. 6. Currents as functions of the fluxes: (a) i_{d}; (b) i_{q}. The mesh surfaces correspond to the fitted model (12). The red stars show the measured samples from the self-axis saturation tests, cf. Fig. 3. The blue circles show the measured samples from the cross-saturation test, cf. Fig. 4.

IV. EXPERIMENTAL RESULTS

A. Fitting

Using the proposed method, the magnetic model (12) was fitted to the measured current and flux samples, shown in Figs. 3 and 4 in the time domain. When $\hat{R}_{\mathrm{s}}$ = 3.6 Ω is used, the fitted parameters are given in Table II. Fig. 6 shows the mesh surfaces, which have been plotted using the fitted parameters in the model (12). Also the measured samples are shown in Fig. 6.

Fig. 7 compares the fitted model with the reference data from the constant-speed method [4]. It can be seen that the fitted model for $\hat{R}_{\mathrm{s}}$ = 3.6 Ω matches very well with real saturation characteristics also in the cross-saturation region. The results for $\hat{R}_{\mathrm{s}}$ = 0 are also shown; it can be seen that the method is comparatively robust against the stator resistance error.

As a comparison, the method [13] would need tens of parameters to model the cross-saturation and separate post-processing and interpolation algorithms should be implemented. On the contrary, only one parameter, a_{dq}, is needed in the proposed method to model the effect of the cross-saturation (since the exponents U = 1 and V = 0 can be typically used). The application of the proposed model and identification method is also more straightforward.

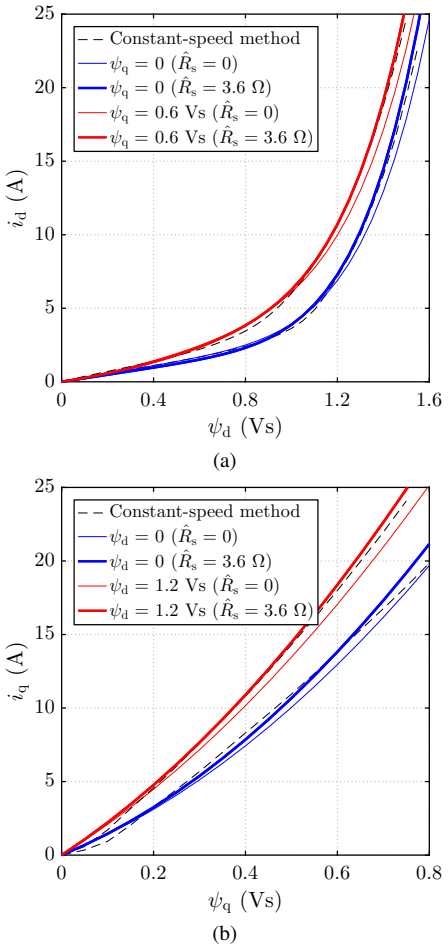

Fig. 7. Currents as functions of the fluxes: (a) i_d as a function of ψ_d for ψ_q = 0 and ψ_q = 0.6 Vs; (b) i_q as a function of ψ_q for ψ_d = 0 and ψ_d = 1.2 Vs. The dashed lines show the reference data, which has been measured using constant-speed identification. The solid lines show the results from the proposed standstill method.

B. MTPA as an Application Example

Fig. 8(a) shows three MTPA trajectories for the motor under test. The stars represent the reference MTPA trajectory, measured using the constant-speed method. The red line shows the MTPA trajectory calculated using the magnetic model (12) and the fitted parameters in Table II. The blue dashed line represents the trajectory, which is also calculated using the model (12), but the cross-saturation is omitted by setting a_{dq} = 0. It can be seen that the proposed method gives a trajectory, which is very close to the reference one. Fig. 8(b) compares the torque factors related to these three trajectories. The torque factor corresponding to the proposed method agrees very well with the the reference trajectory, also in overload conditions.

It is also worth noticing that the magnetic model (12) has been used in sensorless control, e.g., in [15], [19], [20]. Hence, the proposed self-commissioning method can be directly used in connection with these methods.

V. Discussion

Only experimental results were shown in the previous sections. Here, we elaborate on some robustness aspects of the proposed identification method by means of simulations.

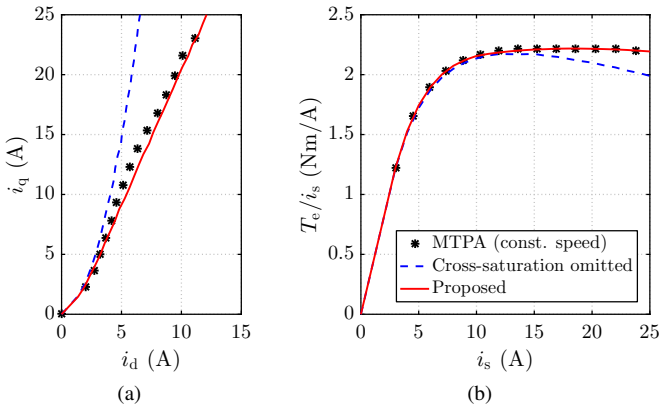

Fig. 8. Comparison of MTPA characteristics: (a) control trajectories; (b) torque factors. The legends given in (b) hold for (a) as well. The current magnitude is denoted by i_s. The stars show the reference data from the constant-speed method. The red solid curves are calculated using the model (12) and the fitted parameters. In the case of the blue dashed curves, the cross-saturation is omitted by setting a_{dq} = 0.

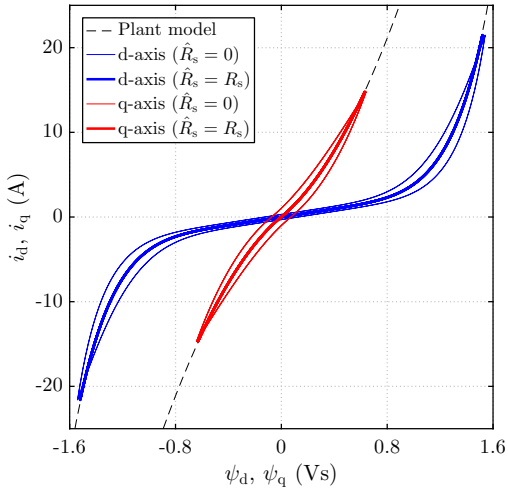

Fig. 9. Simulated self-axis saturation characteristics, corresponding to the experimental results in Fig. 5.

The saturation of the 2.2-kW SyRM is modeled using (12) with the parameters in Table II. The core losses are omitted. The actual stator resistance is R_s = 3.6 Ω. The inertia of the rotor is 0.007 kgm^2 and the mechanical friction is omitted. The sensorless controller and the computational delay are modelled according to Fig. 2.

A. Self-Axis Characteristics

Fig. 9 shows the simulation results from the self-axis standstill tests, corresponding to the experimental results in Fig. 5. It can be seen that using $\hat{R}_s$ = 0 widens the hysteresis loop, similarly to the experiment. The hysteresis loop disappears in the ideal case $\hat{R}_s = R_s$, since the core losses and inverter nonlinearities are not included in the simulation model.

B. Rotor Position Variation

The cross-saturation test was simulated using two different test-voltage magnitudes. The results for $u_{d,out} = u_{q,out}$ = 100 V are shown in Fig. 10(a) and the results for $u_{d,out}$

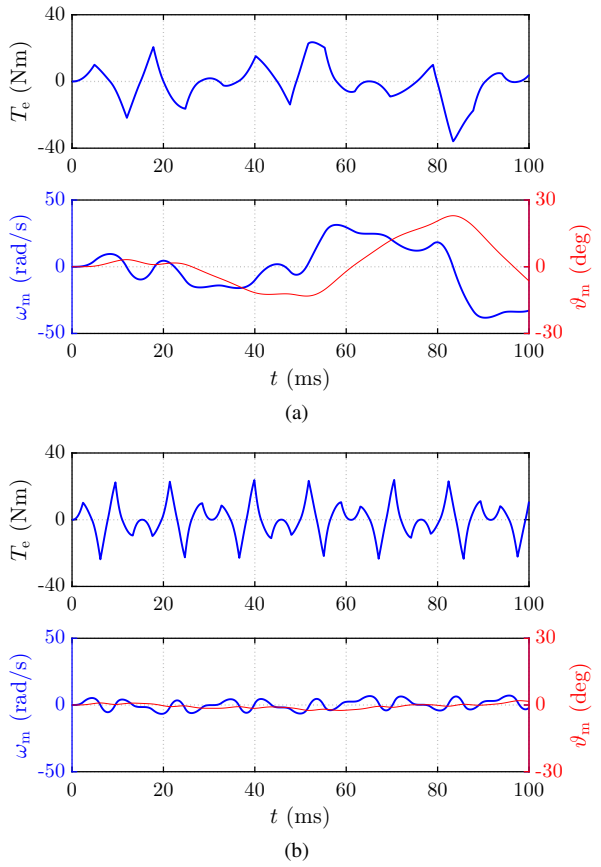

Fig. 10. Simulated cross-saturation test at two different voltages: (a) $u_{d,out}$ = $u_{q,out}$ = 100 V; (b) $u_{d,out}$ = $u_{q,out}$ = 200 V, corresponding to the measurement results shown in Fig. 4. The torque, electrical rotor speed, and rotor angle in electrical degrees are shown.

= $u_{q,out}$ = 200 V in Fig. 10(b). Otherwise, the parameters correspond to the measurement shown in Fig. 4. The torque T_e, rotor speed ω_m (in electrical rad/s), and rotor angle ϑ_m (in electrical degrees) are shown. It can be seen that the position variation is less than three electrical degrees for the 200-V test voltage while it is almost 30 electrical degrees for the 100-V test voltage. For the given machine, the time needed for the cross-saturation test is much below 100 ms shown in the figure. As mentioned before, bigger machines have higher per-unit rotor inertia, reducing the rotor movement during the test.

C. Robustness Against the Rotor Position Variation and Stator Resistance Errors

The magnetic model (12) was fitted using the simulated data from the standstill tests. The test conditions equal those used in the experiments. The resulting fitted model is depicted in Fig. 11, corresponding to the experimental results in Fig. 7. In the case $\hat{R}_s = R_s$, the saturation characteristics of the identified magnetic model almost perfectly overlap with the plant-model characteristics. The small, hardly visible, error originates mainly from the rotor angle variation during the cross-axes test, cf. Fig. 10. The case $\hat{R}_s = 0$ agrees well with the experimental results and confirms the robustness against the stator resistance error.

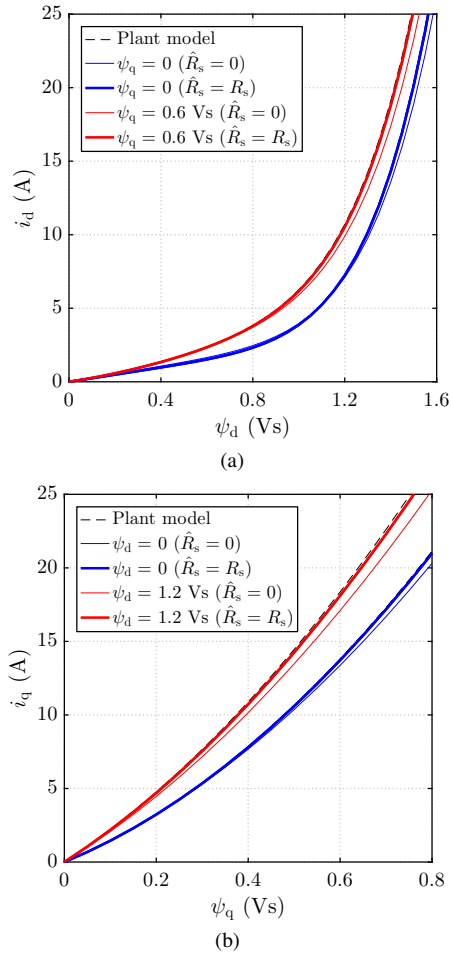

Fig. 11. Simulation results from the proposed standstill method, corresponding to the experimental results in Fig. 7: (a) i_d as a function of ψ_d for $\psi_q = 0$ and $\psi_q = 0.6$ Vs; (b) i_q as a function of ψ_q for $\psi_d = 0$ and $\psi_d = 1.2$ Vs. The dashed lines show the reference data (plant model).

VI. Conclusion

The identification method proposed in this paper combines the test sequence of [13], the algebraic magnetic model of [15], and the LLS method to determine the saturation characteristics of SyRMs at standstill. The cross-saturation effect is included. The method is robust against errors in the stator resistance and inverter voltage, due to the high test voltages. The algebraic magnetic model is physically feasible, it has few parameters, it takes the cross-saturation inherently into account, and it enables extrapolation outside the measured data range. The accuracy of the method has been compared with the reference data from constant-speed identification. The fitted model matches very well with real saturation characteristics also in the cross-saturation region. The proposed method can be used for automatic self-commissioning of sensorless SyRM drives.

References

[1] M. Ruff and H. Grotstollen, "Off-line identification of the electrical parameters of an industrial servo drive system," in *Conf. Rec. IEEE-IAS Annu. Meeting*, vol. 1, San Diego, CA, Oct. 1996, pp. 213–220.

[2] L. Peretti and M. Zigliotto, "Automatic procedure for induction motor parameter estimation at standstill," *IET Electr. Power Appl.*, vol. 6, no. 4, pp. 214–224, Apr. 2012.

[3] K. M. Rahman and S. Hiti, "Identification of machine parameters of a synchronous motor," *IEEE Trans. Ind. Appl.*, vol. 41, no. 2, pp. 557–565, Mar./Apr. 2005.

[4] E. Armando, R. Bojoi, P. Guglielmi, G. Pellegrino, and M. Pastorelli, "Experimental identification of the magnetic model of synchronous machines," *IEEE Trans. Ind. Appl.*, vol. 49, no. 5, pp. 2116–2125, Sept. 2013.

[5] G. Pellegrino, B. Boazzo, and T. Jahns, "Magnetic model self-identification for PM synchronous machine drives," *IEEE Trans. Ind. Appl.*, vol. 51, no. 3, pp. 2246–2254, May 2015.

[6] B. Štumberger, G. Štumberger, D. Dolinar, A. Hamler, and M. Trlep, "Evaluation of saturation and cross-magnetization effects in interior permanent-magnet synchronous motor," *IEEE Trans. Ind. Appl.*, vol. 39, no. 5, pp. 1264–1271, Sept./Oct. 2003.

[7] G. Štumberger, T. Marčič, B. Štumberger, and D. Dolinar, "Experimental method for determining magnetically nonlinear characteristics of electric machines with magnetically nonlinear and anisotropic iron core, damping windings, and permanent magnets," *IEEE Trans. Magn.*, vol. 44, no. 11, pp. 4341–4344, Nov. 2008.

[8] L. Peretti, P. Sandulescu, and G. Zanuso, "Self-commissioning of flux linkage curves of synchronous reluctance machines in quasi-standstill condition," *IET Electr. Power Appl.*, vol. 9, no. 9, pp. 642–651, 2015.

[9] D. Uzel and Z. Peroutka, "Optimal control and identification of model parameters of traction interior permanent magnet synchronous motor drive," in *Proc. IEEE IECON 2011*, Melbourne, Australia, Nov. 2011, pp. 1960–1965.

[10] S. Ebersberger and B. Piepenbreier, "Identification of differential inductances of permanent magnet synchronous machines using test current signal injection," in *Proc. SPEEDAM 2012*, Sorrento, Italy, June 2012, pp. 1342–1347.

[11] I. Omrane, E. Etien, O. Bachelier, and W. Dib, "A simplified least squares identification of permanent magnet synchronous motor parameters at standstill," in *Proc. IEEE IECON 2013*, Vienna, Austria, Nov. 2013, pp. 2578–2583.

[12] S. Odhano, R. Bojoi, S. Rosu, and A. Tenconi, "Identification of the magnetic model of permanent-magnet synchronous machines using DC-biased low-frequency AC signal injection," *IEEE Trans. Ind. Appl.*, vol. 51, no. 4, pp. 3208–3215, July 2015.

[13] N. Bedetti, S. Calligaro, and R. Petrella, "Stand-still self-identification of flux characteristics for synchronous reluctance machines using novel saturation approximating function and multiple linear regression," *IEEE Trans. Ind. Appl.*, vol. 52, no. 4, pp. 3083–3092, July/Aug. 2016.

[14] M. Hinkkanen, P. Pescetto, E. Mölsä, S. E. Saarakkala, G. Pellegrino, and R. Bojoi, "Sensorless self-commissioning of synchronous reluctance motors at standstill," in *Proc. ICEM 2016*, Lausanne, Switzerland, Sept. 2016, pp. 1176–1182.

[15] Z. Qu, T. Tuovinen, and M. Hinkkanen, "Inclusion of magnetic saturation in dynamic models of synchronous reluctance motors," in *Proc. ICEM'12*, Marseille, France, Sept. 2012, pp. 994–1000.

[16] A. Vagati, M. Pastorelli, F. Scapino, and G. Franceschini, "Impact of cross saturation in synchronous reluctance motors of the transverse-laminated type," *IEEE Trans. Ind. Appl.*, vol. 36, no. 4, pp. 1039–1046, July/Aug. 2000.

[17] H. C. J. de Jong, "Saturation in electrical machines," in *Proc. ICEM'80*, vol. 3, Athens, Greece, Sept. 1980, pp. 1545–1552.

[18] T. Söderström and P. Stoica, *System Identification*. Hemel Hempstead, UK: Prentice Hall International, 1989. [Online]. Available: http://user.it.uu.se/~ts/sysidbook.pdf

[19] T. Tuovinen and M. Hinkkanen, "Adaptive full-order observer with high-frequency signal injection for synchronous reluctance motor drives," *IEEE J. Emerg. Sel. Topics Power Electron.*, vol. 2, no. 2, pp. 181–189, June 2014.

[20] H. A. A. Awan, T. Tuovinen, S. E. Saarakkala, and M. Hinkkanen, "Discrete-time observer design for sensorless synchronous motor drives," *IEEE Trans. Ind. Appl.*, vol. 52, no. 5, pp. 3968–3979, Sept./Oct. 2016.